Supplementary Information

Mechanistic study of immobilised molecular electrocatalyst by in-situ gap plasmon assisted spectro-electrochemistry

Demelza Wright[1,2,6], Qianqi Lin[1,6], Dénes Berta[3,4], Tamás Földes[3,4], Andreas Wagner[2], Jack Griffiths[1], Charlie Readman[1,5], Edina Rosta[3,4*], Erwin Reisner[2*], Jeremy J. Baumberg[1*]

[1]Nanophotonics Centre, Department of Physics, Cavendish Laboratory, University of Cambridge, Cambridge, CB3 0HE, England, UK

[2]Department of Chemistry, University of Cambridge, Lensfield Road, Cambridge CB2 1EW, Cambridge, UK

[3]Department of Chemistry, King's College London, 7 Trinity Street, London SE1 1DB, UK

[4]Department of Physics and Astronomy, University College London, London WC1E 6BT, UK

[5]Melville Laboratory for Polymer Synthesis, Department of Chemistry, University of Cambridge, Lensfield Road, Cambridge CB2 1EW, UK

[6]These authors contributed equally: Demelza Wright and Qianqi Lin.

*e-mail: e.rosta@ucl.ac.uk; reisner@ch.cam.ac.uk; jjb12@cam.ac.uk

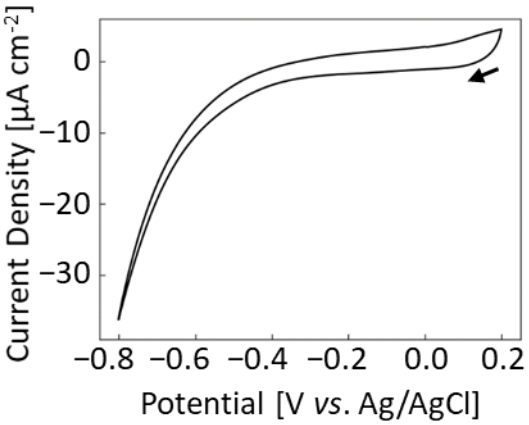

Supplementary Fig. 1 | Cyclic voltammogram of PDI monolayer in NPoM construct in N_2-saturated 0.1 M aqueous KCl. Arrow indicates scan start direction, scan rate = 100 mV s^{-1}.

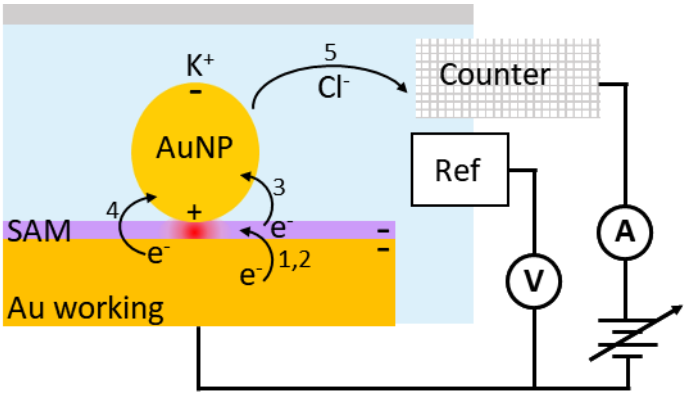

Supplementary Fig. 2 | Conduction pathways in the spectro-electrochemical cell. 1. Non-Faradaic/capacitive charging. 2. Faradaic electron transfer, only applies to redox active SAM. 3. Electron conduction. 4. Electron tunnelling. 5. Electric current flows by movement of ions.

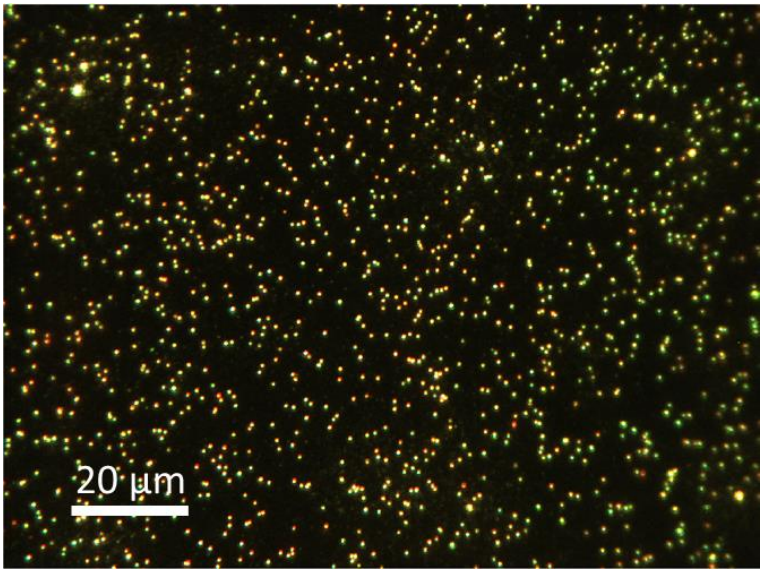

Supplementary Fig. 3 | Dark-field image of **Ni(tpyS)$_2$** monolayer NPoM construct, taken with a 100x, 0.8 NA objective. NPoM diameter = 60 nm. NPoM scattering diameter = 950 nm. Surface coverage of scattering NPoMs = 7%, from measurements using ImageJ.[1] Surface coverage of actual NPoMs = 0.03 %, calculated from $(60/2)^2/(950/2)^2 \times 7\%$.

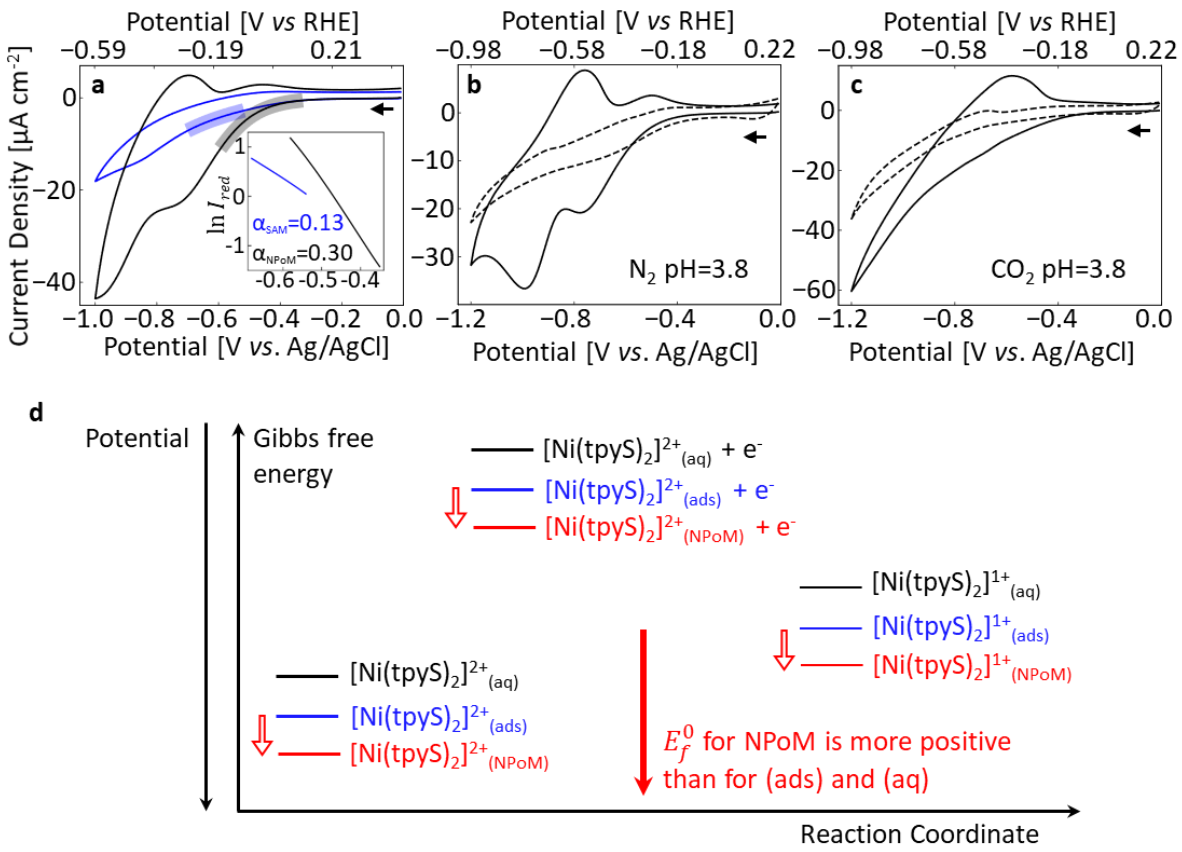

Supplementary Fig. 4 | Cyclic voltammograms of **Ni(tpyS)$_2$** monolayer. **a**, **Ni(tpyS)$_2$** monolayer before (blue) and after (black) AuNP deposition. N_2-saturated 0.1 M KCl electrolyte at pH=7. Inset: Tafel plot for highlighted regions. α is the transfer coefficient (ranging from 0 to 1, representing reaction intermediate is reactant-like and product-like, respectively) for **red1**. Tafel analysis shows reduction is thermodynamically more favourable when AuNP is on top of the SAM. **b**-**c**, **Ni(tpyS)$_2$** monolayer in NPoM construct (solid lines) with comparison to bare Au (dashed lines). **b**, N_2-saturated 0.1 M KCl/HCl electrolyte at pH=3.8. **c**, CO_2-saturated 0.1 M KCl at pH=3.8. Arrow indicates scan start direction. Scan rate = 100 mV s^{-1}. **d**, Gibbs energy diagram of **Ni(tpyS)$_2$** in solution phase (aq), adsorption phase (ads), and NPoM phase (NPoM).

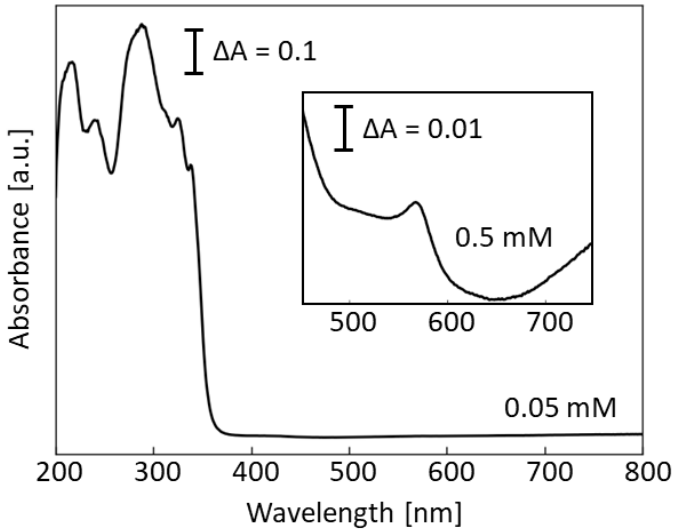

Supplementary Fig. 5 | UV-Visible spectra of **Ni(tpyS)$_2$** in acetonitrile. Two concentrations (0.05 mM and 0.5 mM inset) are shown to emphasise details of UV and visible regions. Spectra are referenced to absorbance of pure acetonitrile.

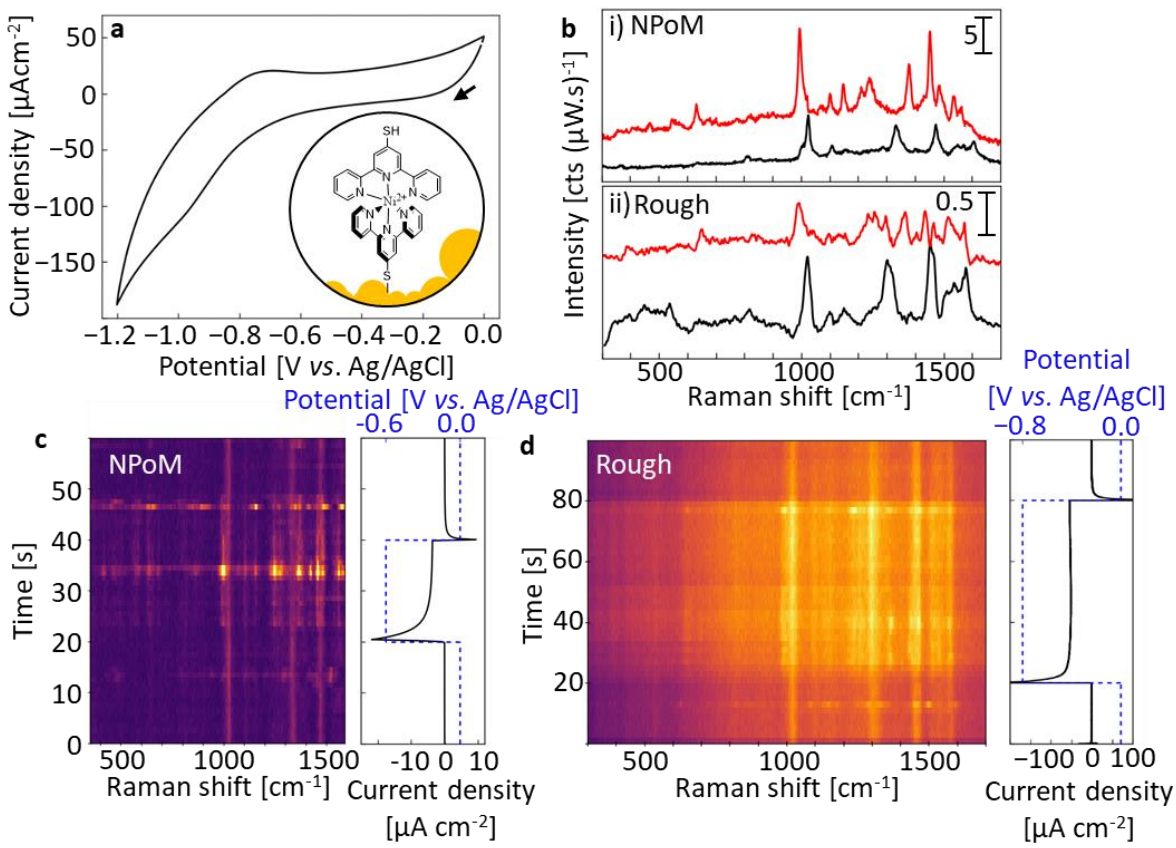

Supplementary Fig. 6 | Spectro-electrochemistry of **Ni(tpyS)$_2$** monolayer on an electrochemically roughened gold electrode *vs.* NPoM. **a**, Cyclic voltammogram of **Ni(tpyS)$_2$** monolayer on rough gold. Arrow indicates scan start direction. Scan rate = 100 mV s^{-1}. **b**, Potential dependent SERS spectra of (i) **Ni(tpyS)$_2$** in NPoM at 0 V (black) and −0.6 V (red). Same data as main text (**Fig. 3a**) included to allow direct comparison with (ii) **Ni(tpyS)$_2$** on rough gold at 0 V (black) and −0.8 V (red). Spectra in red are difference spectra for clarity. **c**, Consecutive NPoM SERS spectra with real-time chronoamperometry corresponding to spectra in **b** (i). **d**, Consecutive roughened gold SERS spectra with real-time chronoamperometry corresponding to spectra in **b** (ii). All electrochemical data are obtained in N_2-saturated 0.1 M KCl electrolyte at pH=7.

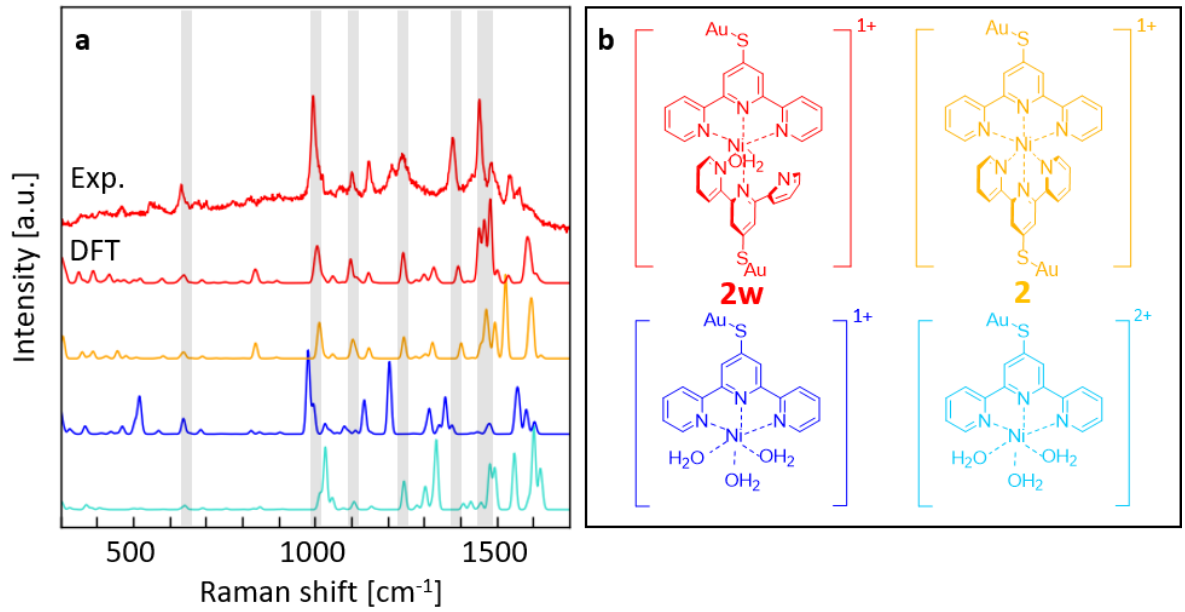

Supplementary Fig. 7 | DFT calculated SERS spectra for **Ni(tpyS)$_2$** reduced singly in N_2 conditions compared to experimental spectrum. **a**, Spectra offset in vertical axis for clarity, shaded lines to guide the eye. **b**, Structures corresponding to spectra in **a**. Relative Gibbs free energies of structures **2w** and **2** are shown in **Fig. S11c**.

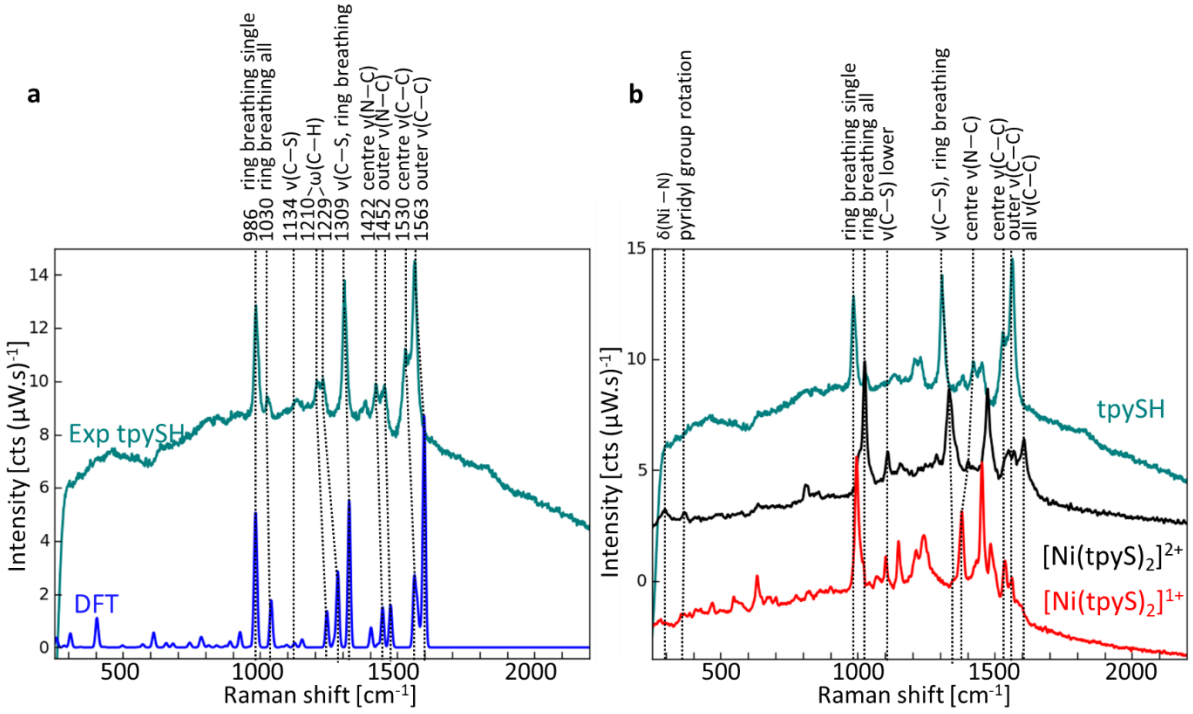

Supplementary Fig. 8 | Raman and DFT calculated spectra for **tpySH** ligand. **a**, Powder Raman spectrum of tpySH ligand (cyan) and DFT calculation (blue). Relevant modes in DFT and experiment are matched by dashed lines as a guide to the eye. **b**, Powder Raman spectrum of tpySH from **a** (cyan), in comparison with SERS spectra of $[Ni(tpyS)_2]^{2+}$ and $[Ni(tpyS)_2]^{1+}$ from **Fig. 3a** (black and red). Dashed lines connect the related modes in each spectrum.

Supplementary Note 1 | Changes of bands with potential

We compare the most relevant modes in $[Ni(tpyS)_2]^{2+}$ and $[Ni(tpyS)_2]^{1+}$ experimental spectra (Supplementary **Fig. 8b**). Working from low to high wavenumber: ν(Ni−N) is well defined for $[Ni(tpyS)_2]^{2+}$, whereas the mode is broader for $[Ni(tpyS)_2]^{1+}$, reflecting the change in Ni-N bond strengths and loss of symmetry after reduction and water coordination. The Raman cross section of ν(Au−S) ~ 330 cm^{-1} is too low to be detected. A similar trend as for ν(Ni −N) is observed for the pyridyl group rotation. Ring breathing modes at 986 cm^{-1} and 1030 cm^{-1} are attributed to individual and collective pyridyl vibrations, respectively. The individual pyridyl mode dominates in the free ligand and water-coordinated $[Ni(tpyS)_2]^{1+}$, while for $[Ni(tpyS)_2]^{2+}$ the collective mode is more intense, again reflecting the higher degree of symmetry in the latter structure. ν(C−S) redshifts from the free ligand to the $[Ni(tpyS)_2]^{2+}$ complex, likely dominated by Au coordination to the thiol group. For the $[Ni(tpyS)_2]^{1+}$ complex, this mode splits into two. One component is not shifted significantly compared to $[Ni(tpyS)_2]^{2+}$, while the other is blue-shifted to 1148 cm^{-1}. A new ν(C−C) mode ~1600 cm^{-1} appears for $[Ni(tpyS)_2]^{2+}$ due to delocalisation of vibrations in the symmetric molecule and is significantly diminished in the $[Ni(tpyS)_2]^{1+}$ spectrum. Mode positions for centre and outer ν(C−C) are similar for the free ligand and $[Ni(tpyS)_2]^{1+}$, but intensities differ significantly.

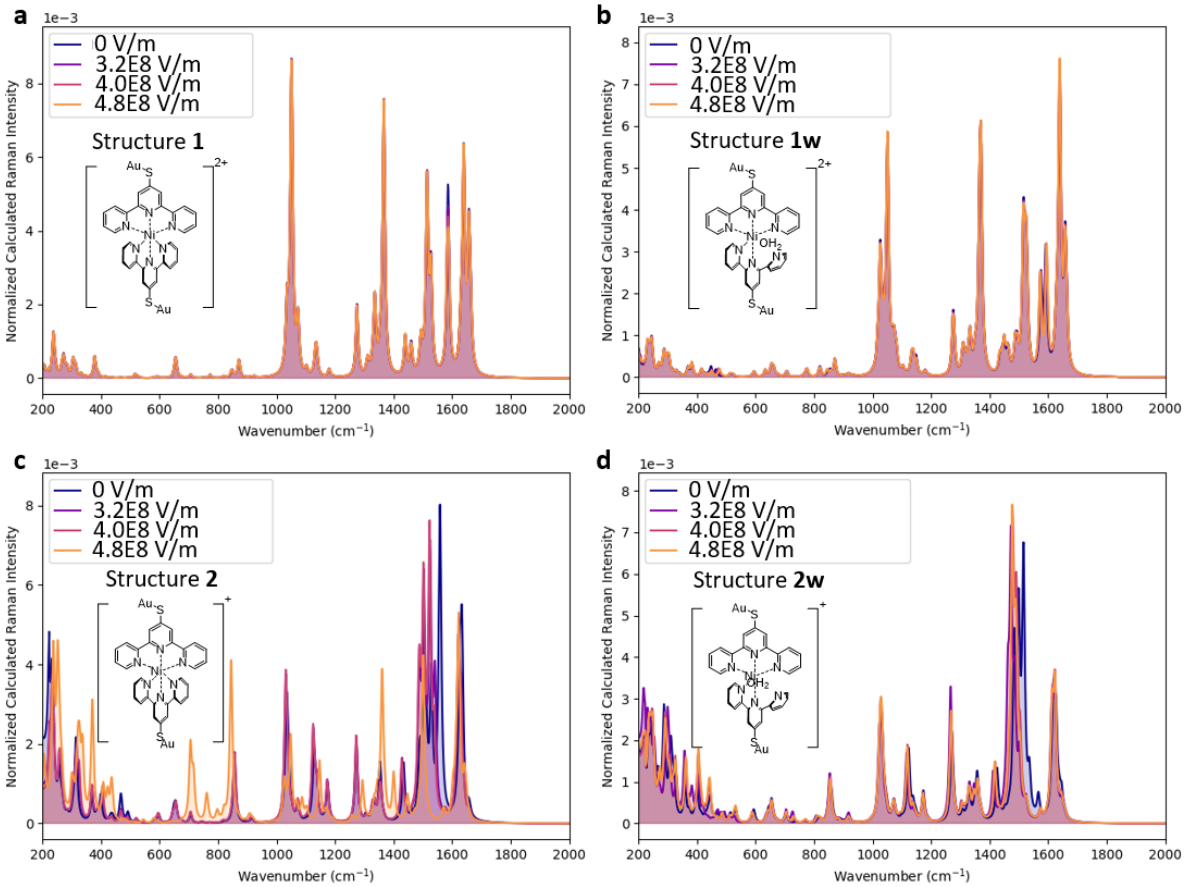

Supplementary Fig. 9 | Calculated DFT calculated spectra for **Ni(tpyS)$_2$** with polarization effects on dipoles at different electric field strength. **a**, Structure **1** = $[Ni(tpyS)_2]^{2+}$. **b**, Structure **1w** = $[Ni(tpyS)_2\text{-}H_2O]^{2+}$. **c**, Structure **2** = $[Ni(tpyS)_2]^{1+}$. **d**, Structure **2w** = $[Ni(tpyS)_2\text{-}H_2O]^{1+}$.

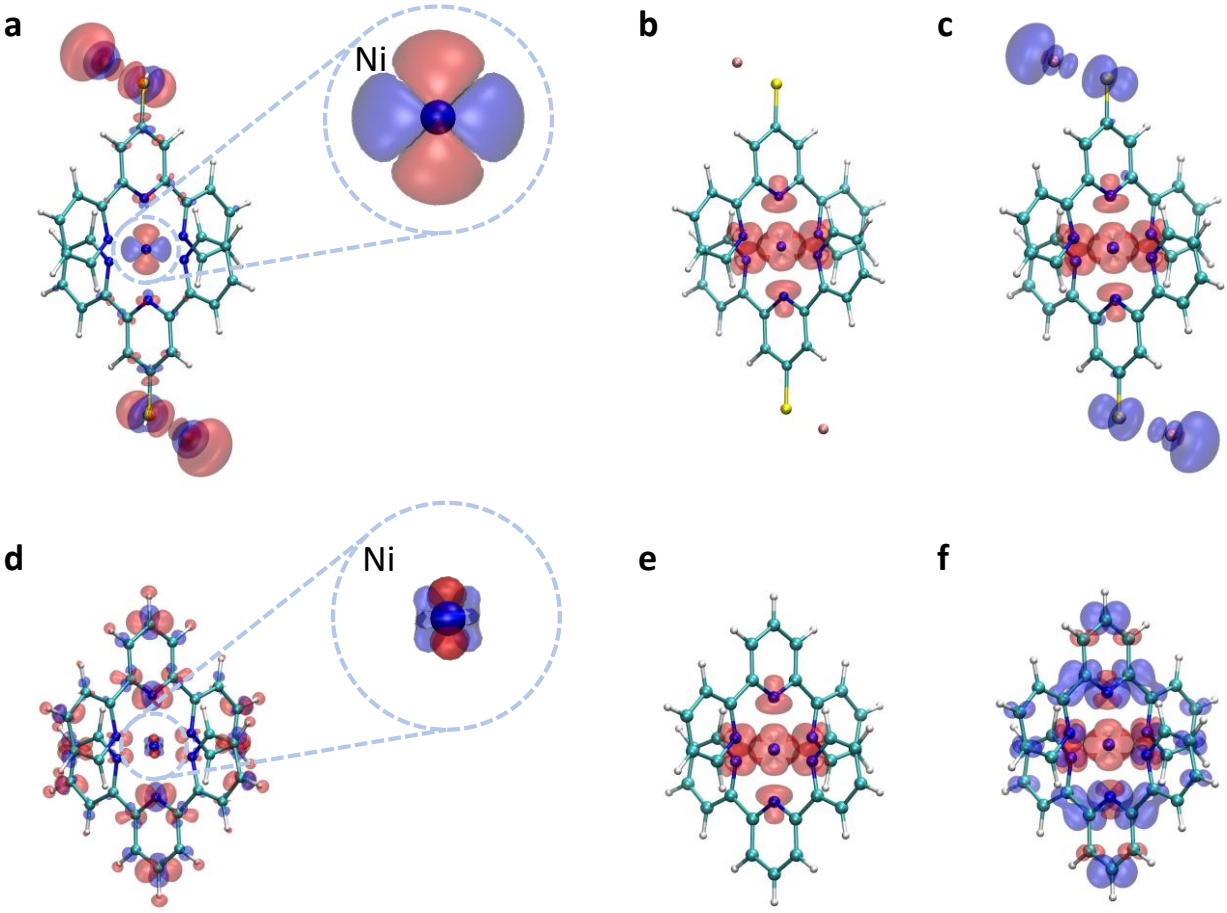

Supplementary Fig. 10 | Electron and spin densities for Ni(tpyS)$_2$ and Ni(tpy)$_2$, upper and lower respectively. All plots depict iso-surfaces for ±0.002 Au electron densities. **a**, Total electron density change for the reduction from $[Ni(tpyS)_2]^{2+}$ to $[Ni(tpyS)_2]^{1+}$. **b**, Spin density in $[Ni(tpyS)_2]^{2+}$. **c**, Spin density in $[Ni(tpyS)_2]^{1+}$. **d**, Total electron density change for the reduction of $[Ni(tpy)_2]^{2+}$ to $[Ni(tpy)_2]^{1+}$. **e**, Spin density in $[Ni(tpy)_2]^{2+}$. **f**, Spin density in $[Ni(tpy)_2]^{1+}$. Red: Increased electron density region. Blue: Decreased electron density region.

Supplementary Table 1 | Wiberg bond indices[2–4] for Ni-N coordination bonds in $[Ni(tpyS)_2]^{2+}$ and $[Ni(tpyS)_2]^{1+}$.

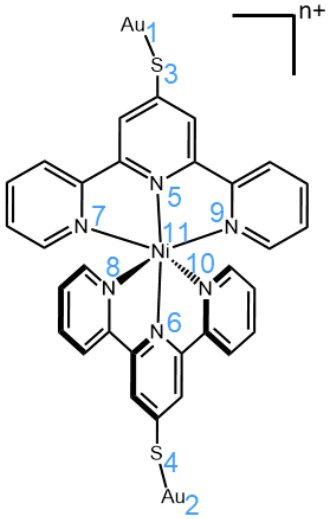

Bonds	Wiberg bond index		Change
	$[Ni(tpyS)_2]^{2+}$	$[Ni(tpyS)_2]^{1+}$	
$Au_1 - S_3$	0.952	0.630	−0.322
$Au_2 - S_4$	0.952	0.630	−0.322
$Ni - N_5$	0.300	0.314	+0.014
$Ni - N_6$	0.300	0.314	+0.014
$Ni - N_7$	0.263	0.260	−0.003
$Ni - N_8$	0.261	0.268	+0.007
$Ni - N_9$	0.261	0.268	+0.007
$Ni - N_{10}$	0.263	0.261	−0.002

Supplementary Note 2 | Earth mover's algorithm

To evaluate the spectral match of all considered species against the experimental SERS spectrum obtained in reduction conditions at -0.8 V, all spectra represented in the 400-2500 cm^{-1} window were sampled at integer wavenumbers. The experimental spectrum was also baseline corrected. The computational intensities R_i were calculated as follows:

$$\mathrm{R_i} = \frac{2\pi^4}{45}(\nu_0 - \nu_i)^4 \cdot \frac{h}{8\pi^2 c\nu_i\left(1 - \exp\left(-\frac{h\nu_i c}{kT}\right)\right)} \cdot S_i \qquad (1)$$

Here, for vibrational mode i with frequency ν_i, the Raman activity is S_i, ν_0 is the frequency of the probing light, h is the Planck constant, c is the speed of light, k is the Boltzmann constant and T is room temperature at 298 K. Calculated frequencies were scaled by the factor of 0.978. The computational spectra were obtained by broadening the peaks using Gaussian functions of 10 cm^{-1} variance.

We have defined the distance between two spectra using the Earth mover's algorithm[5,6]:

$$d(X,Y) = \sum_{i=1}^{n}\left|\sum\nolimits_{j=1}^{i} x_j - \sum\nolimits_{j=1}^{i} y_j\right| \qquad (2)$$

where X and Y are the intensity vectors defined in the same range. While Y was kept as the experimental reference, X was defined as $\sum_{i=1}^{m} c_i Z_i$, where $m = 1, 2, 3$ and Z_i refers to computational spectra and c_i are calculated to minimize d.

To compare the computed spectra from a single species ($m = 1$) to the experimental spectrum, **2w** is the closest thermodynamically accessible species, with the smallest distance (Supplementary **Fig. 13a**). We also considered the presence of multiple species using a linear combination of 2 or 3 intermediates. We again discarded thermodynamically unfavourable species, and optimised the scaling factors (c_i) in the linear combination to minimise the overall distance from the experimental reference. The best match is a mixture of **4b** and **2w** species (Supplementary **Fig. 13**). Attempts with combining three spectra did not lead to further improvement, and was not considered further.

The semi-quantitative analysis of vibrational spectra provides the basis of the suggested catalytic cycle in **Fig. 4b**. Note that not all reaction intermediates may be observed experimentally in the captured Raman spectra, due to e.g. their short lifetime.

Supplementary Note 3 | Reaction intermediate calculations

A series of intermediates were considered during the reduction process, including Ni-centred complexes from ref 7. Upon the complete CO_2 reduction, two protons and two electrons are transferred to the complex. The calculated species are organised by taking into account all possibilities for these transfer steps to proceed stepwise or concerted (Supplementary **Table 2**).

Supplementary Table 2 | Classification of each numbered intermediate in **Fig. S11** along protonation and redox steps. Note that species **1** and **2** do not include a CO_2 molecule. Species in red denote thermodynamically unfavourable species (Supplementary **Fig. 11**).

	+0 H^+	+1 H^+	+2 H^+
+0 e^-	**1, 1w**	**7a-b**	
+1 e^-	**2, 2w**	**3a-d**	**5, 5b, 8a-c**
+2 e^-		**4a-c**	**6, 6b, 9a-c**

We used the experimental potential to account for the free energy changes in the redox steps and an energy difference of 269.2 kcal mol^{-1} to account for the cost of protonation. This value corresponds to a pH of 3.8 and the energy of a proton[8]. The diagonal elements of Supplementary **Table 2** correspond to intermediates obtained via concerted electron-proton transfers. In the upper triangular elements, the proton transfer precedes the reduction step, which was found highly endergonic in our DFT calculations (Supplementary **Fig. 11**). The lower triangular elements, when the protonation takes place after the reduction is energetically more favourable, as also suggested by the good spectral agreement for the compounds **4a-c** (see below).

a + 0 H^+, + 0 e^-

$Ni(tpyS)_2^{2+}$

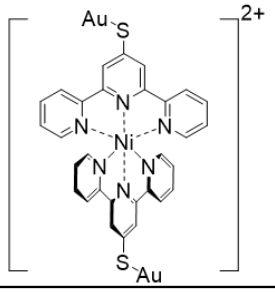

1
0.0
$[L_6\text{-}Ni]^{2+}$

$Ni(tpyS)_2^{2+} + H_2O$

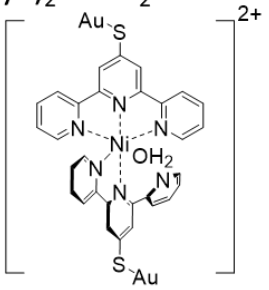

1w
-1.4

b + 1 H^+, + 0 e^-

$Ni(tpyS)_2^{2+} + CO_2 + H^+$

7a
39.8

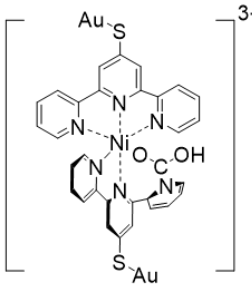

7b
91.5
$[L_5\text{-}Ni\text{-}O\text{-}C\text{-}OH]^+$

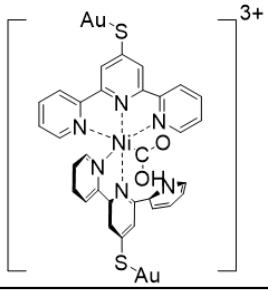

c + 0 H^+, + 1 e^-

$Ni(tpyS)_2^{1+}$

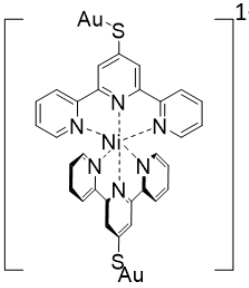

2
-16.9

$Ni(tpyS)_2^{1+} + H_2O$

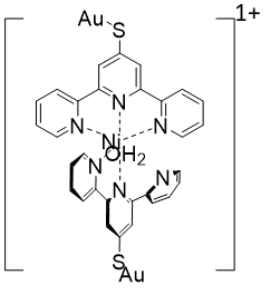

2w
-55.2
$[L_5\text{-}Ni\text{-}OH_2]^+$

d + 1 H^+, + 1 e^-

$Ni(tpyS)_2^{1+} + CO_2 + H^+$

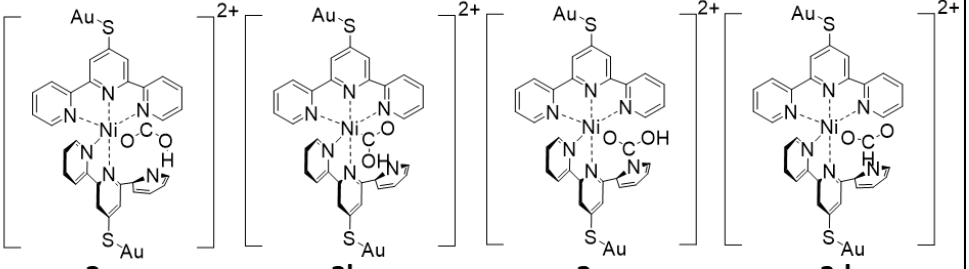

3a -45.7 | **3b** -34.5 | **3c** 38.1 | **3d** -29.0

e + 2 H^+, + 1 e^-

$Ni(tpyS)_2^{1+} + CO_2 + 2H^+$

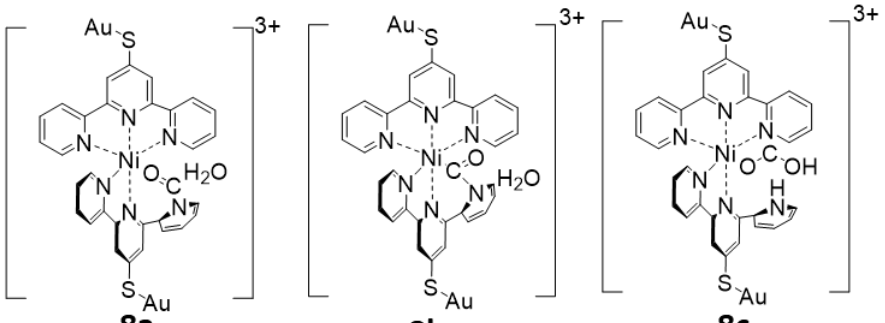

8a 56.1 **8b** -32.2 **8c** -29.6

$Ni(tpyS)_2^{1+} + CO_2 + 2H^+ - H_2O$

5a -36.9

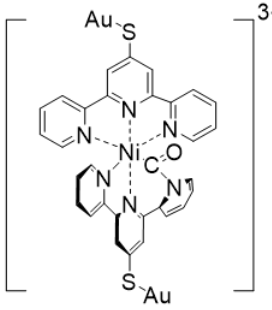

5b -4.2

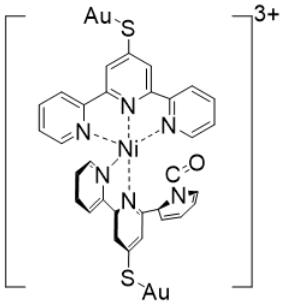

f + 2 H^+, + 2 e^-

$Ni(tpyS)_2^{1+} + CO_2 + e^- + 2H^+$

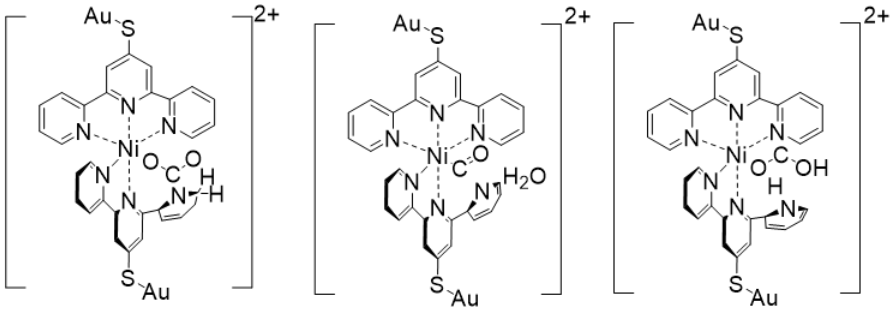

9a -135.4 **9b** -140.3 **9c** -110.3

$Ni(tpyS)_2^{1+} + CO_2 + e^- + 2H^+ - H_2O$

6a -140.9 $[L_5\text{-Ni-C}\equiv\text{O}]^{2+}$

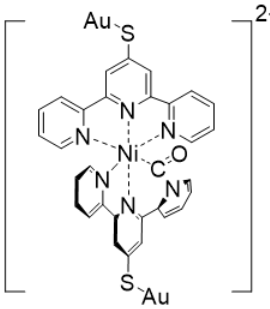

6b -160.3

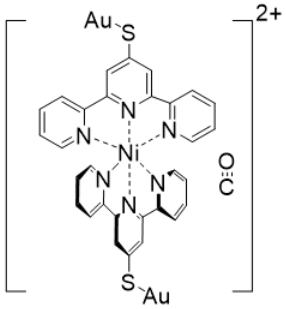

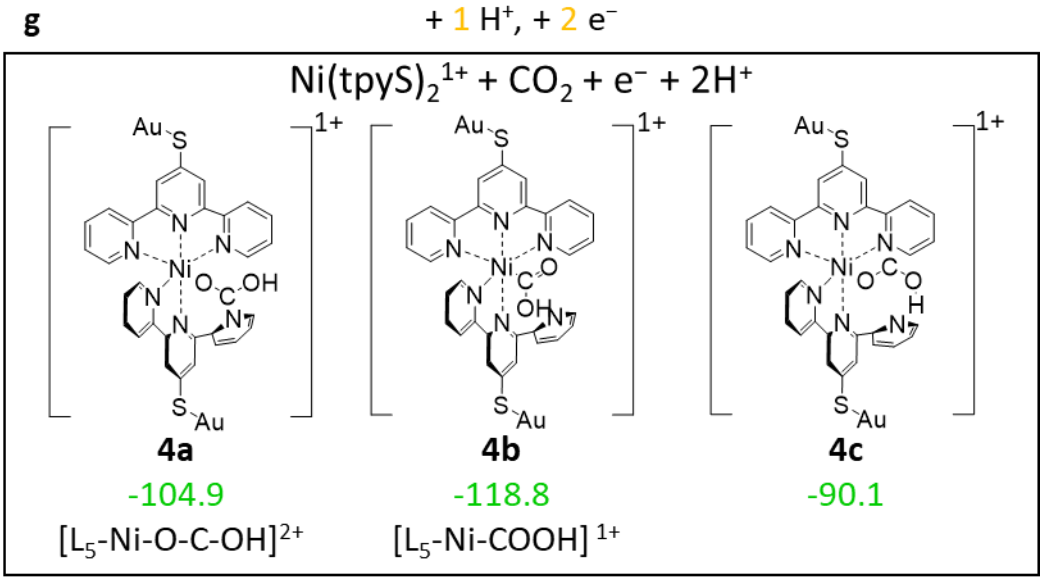

Supplementary Fig. 11 | Computationally screened intermediates considered in CO_2 reduction reactions. Sections **a**-**g** are separated by number of electrons and/or protons (Supplementary **Table 2**). The mechanism presented in **Fig. 4b** uses the best matching computational and experimental Raman spectra. Relative Gibbs free energies (ΔG, green) are shown in kcal mol^{-1}.

Supplementary Table 3 | Calculated total energy components of species discussed in the main text. All values are in hartree. Free energies (last column) are calculated for 1 mol/L concentration and defined as $G = E' + (G_0 - E) + (G_{solv} - E) + 0.00302$.

structure	charge	multiplicity	E	G_0	G_{solv}	E'	G
1	2	3	-4058.521060	-4058.153963	-4058.742643	-4060.606197	-4060.457663
1w	2	3	-4134.881602	-4134.493066	-4135.121270	-4137.083892	-4136.932004
2	1	2	-4058.772499	-4058.408974	-4058.847435	-4060.798258	-4060.506649
2w	1	2	-4135.131577	-4134.745371	-4135.232339	-4137.328239	-4137.039776
3a	2	2	-4247.456896	-4247.072471	-4247.711253	-4249.788136	-4249.655047
3b	2	2	-4247.493541	-4247.103893	-4247.722724	-4249.800748	-4249.637263
3c	2	2	-4247.508074	-4247.116114	-4247.734920	-4249.811148	-4249.643014
3d	2	2	-4247.464936	-4247.076720	-4247.709117	-4249.775534	-4249.628479
4a	1	3	-4247.762127	-4247.375884	-4247.863604	-4250.066535	-4249.778749
4b	1	3	-4247.767960	-4247.385494	-4247.872397	-4250.082001	-4249.800952
4c	1	3	-4247.736058	-4247.353027	-4247.832615	-4250.044710	-4249.755216
5	3	2	-4171.309190	-4170.929441	-4171.767329	-4173.522504	-4173.597874
5b	3	2	-4171.240321	-4170.866895	-4171.702295	-4173.460269	-4173.545797
6	2	3	-4171.727645	-4171.357202	-4171.946875	-4173.947187	-4173.792954
6b	2	3	-4171.754842	-4171.388164	-4171.973048	-4173.975453	-4173.823961
7a	3	3	-4247.123678	-4246.733568	-4247.585372	-4249.428161	-4249.496725
7b	3	3	-4247.044973	-4246.656768	-4247.498331	-4249.352324	-4249.414457
8a	3	2	-4247.643091	-4247.249108	-4248.049834	-4249.912105	-4249.921847
8b	3	2	-4247.697420	-4247.297332	-4248.152941	-4250.010061	-4250.062474
8c	3	2	-4247.690675	-4247.294886	-4248.146908	-4250.000952	-4250.058375
9a	2	3	-4248.128886	-4247.727900	-4248.355310	-4250.434003	-4250.256422
9b	2	3	-4248.110609	-4247.721354	-4248.335624	-4250.431450	-4250.264189
9c	2	3	-4248.077551	-4247.683510	-4248.302443	-4250.388528	-4250.216360
$NiStpy(H_2O)_3^{2+}$	2	3	-3012.253512	-3012.017117	-3012.508771	-3013.690810	-3013.706653
$NiStpy(H_2O)_3^{+}$	1	2	-3012.520105	-3012.287650	-3012.626084	-3013.959361	-3013.829865
water	0	1	-76.358890	-76.355320	-76.370472	-76.467126	-76.472118
CO	0	1	-113.225741	-113.239753	-113.217099	-113.363185	-113.365537
CO_2	0	1	-188.444680	-188.453606	-188.440817	-188.671535	-188.673580

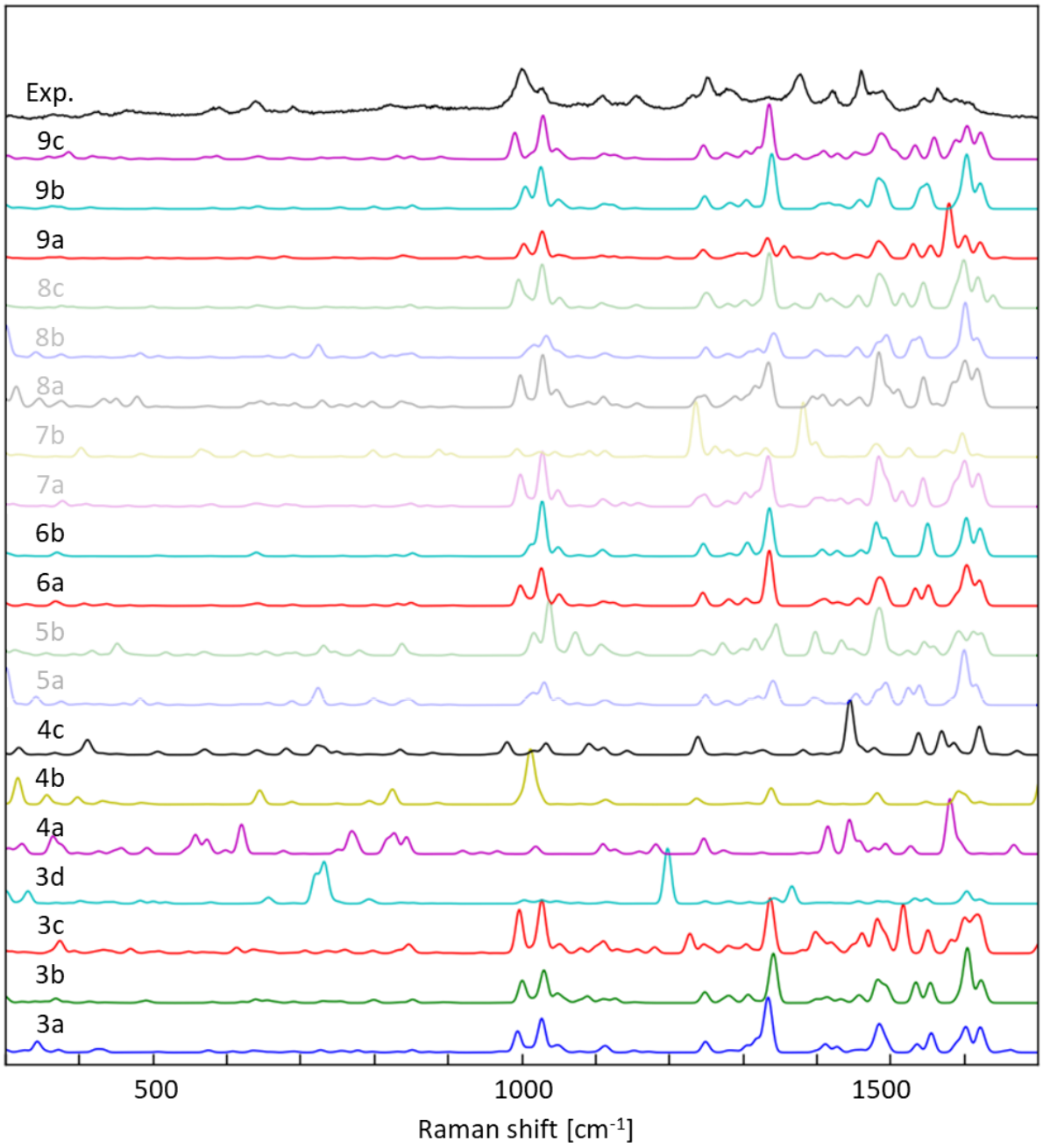

Supplementary Fig. 12 | DFT calculated Raman spectra for **Ni(tpyS)$_2$** during chronoamperometry in CO_2 conditions. Top spectrum is experimental, subsequent spectra are numbered according to structures in Supplementary **Table 3** and Supplementary **Fig. 11**. Shaded spectra are deemed thermodynamically inaccessible.

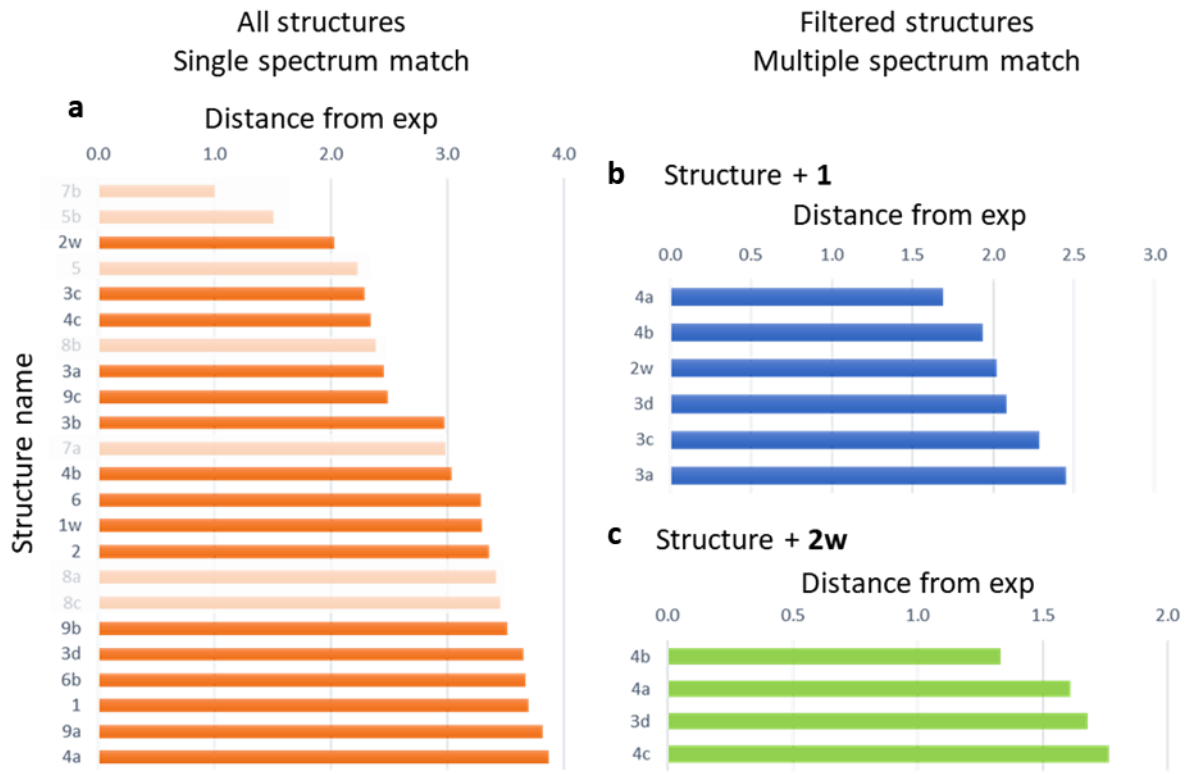

Supplementary Fig. 13 | Earth mover's algorithm output for spectral matching. Lower numbers are a closer match to experiment. All outputs normalised to structure 7b. **a**, Matching result for single spectrum. Shaded structures are deemed thermodynamically inaccessible. **b**, Linear combination of structure **1** with others, highly energetically unfavourable structures are removed. **c**, Linear combination of structure **2w** with others, highly energetically unfavourable structures are removed.

Supplementary Table 4 | Optimal linear combinations for a mixture with intermediates **1** (blue, Supplementary **Fig. 13b**) and **2w** (green, Supplementary **Fig. 13c**) to match SERS spectra at -0.8 V. Matching distance of the individual species alone is also given (D, Supplementary **Fig. 13a**). Ratios are determined as $r_i = c_{i,2}/c_{i,1}$ where $c_{i,m}$ is the scaling factor of spectrum i when the linear combination of m spectra is fitted to the experimental one. Mixture of 75% **2w** and 25% **4b** gives the best spectral match. Energetically unfavourable structures are omitted.

structure	*D*	r_1	r_i
4a	1.69	0.61	0.39
4c	1.94	0.38	0.62
4b	1.94	0.41	0.59
2w	2.02	0.00	1.00
3d	2.08	0.60	0.40
3c	2.29	0.00	1.00
3a	2.45	0.00	1.00

structure	*D*	r_{2w}	r_i
4b	1.33	0.75	0.25
4a	1.61	0.83	0.17
3d	1.68	0.88	0.12
4c	1.77	0.77	0.23
3a	2.02	0.97	0.03

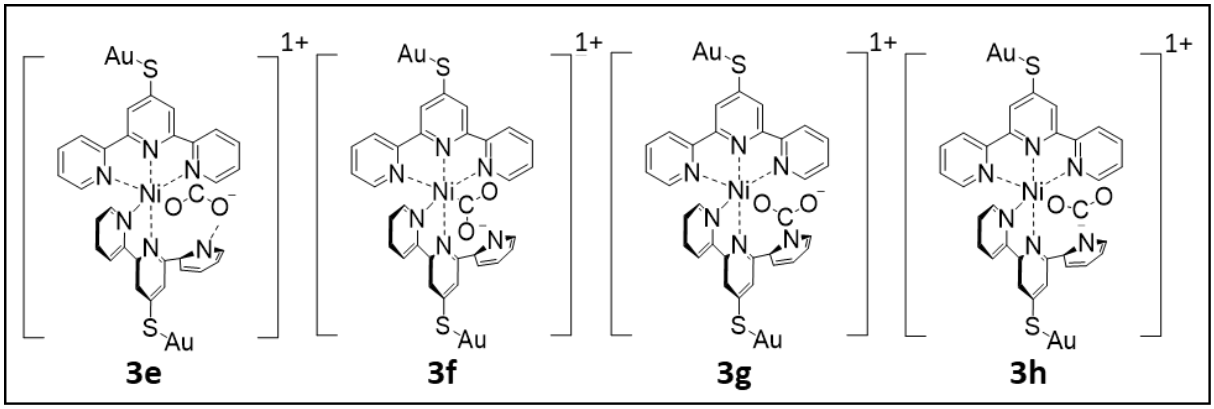

Supplementary Fig. 14 | Intermediates considered in CO_2 reduction reactions with deprotonated carboxyl groups bound to the nickel centre, **3e-h,** corresponding to protonated intermediates **3a-d**, respectively in **Fig. S11d.** During geometry optimization, **3e**, **3f**, and **3h** were not stable because they released the CO_2.

Supplementary Note 4 | pK_a of pendant pyridyl group

We perform additional calculations for pK_a of a complexed terpyridyl group with thiol substitution. The released pendant pyridyl groups in structures **1w** and **2w** were protonated, and their corresponding stabilities and pK_a values were calculated (Supplementary **Table 5**). From these calculations we obtained pK_a values -9.33 and -1.22 for **1w** and **2w**, respectively.

We therefore suggest that the pK_a of complexed substituted terpyridine, and hence the pendant pyridinyl group, is not equivalent to the free unsubstituted ligand in solution.[10] The added proton introduces extra steric demands on the system which can impact the relative stability of the protonated species differently in the immobilized Ni complex compared with the free terpyridine. Consequently, the resulting pK_a values can negatively shift. In an aqueous media with pH=3.8, we therefore expect that only a negligible fraction of these compounds will be protonated.

Supplementary Table 5 | DFT calculations for pK_a of the complexed pendant pyridyl group with thiol substitution in structures **1w** and **2w**, and the free pyridine from literature. *We estimated the ΔG value from the experimental pK_a of the pyridine found in the literature[9].

	ΔG (kcal mol^{-1})	pK_a	Percentage of protonation (at pH=3.8)
1w	12.7	-9.33	0.00%
2w	1.7	-1.22	0.00%
Free pyridine	-7.16*	5.25*	33.65%

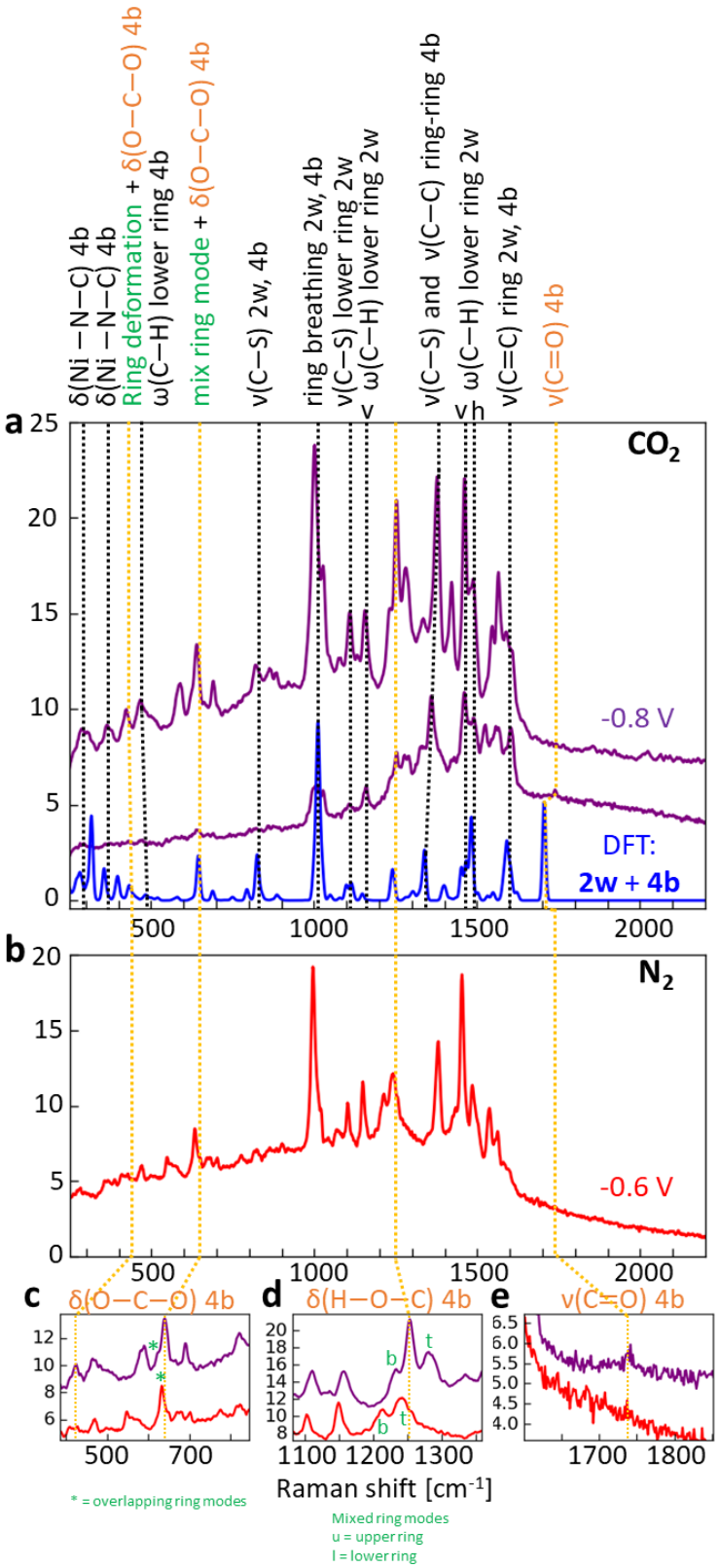

Supplementary Fig. 15 | Comparison of SERS spectra from Ni(tpyS)$_2$ under CO_2 and N_2 saturation. a, SERS (purple, from different NPoMs) and DFT spectra (blue) under CO_2 saturation at −0.8 V. Detailed vibrational modes are matched by dashed lines. Modes relevant to CO_2 reduction are highlighted in orange. **b**, SERS under N_2 saturation at −0.6 V. **c-e**, Comparison of spectra enlarged to show activated CO_2 modes from intermediate **4b**. **c**, δ(O-C-O). * denotes ring deformation mode overlapped with δ(O-C-O). **d**, δ(H-C-O). b and t represent bidentate and tridentate terpyridines modes adjacent to δ(H-C-O). **e**, δ(C=O), which is low intensity and absent from some NPoMs, due to weak enhancement when C=O is perpendicular to the gap optical field (DFT uses unpolarized excitation).

Supplementary Note 5 | Changes of bands with CO_2 atmosphere

Supplementary **Fig. 15** shows a comparison between the intermediate **4b** obtained under CO_2 (Supplementary **Fig. 15a**) and the reduced species **2w** under N_2 (Supplementary **Fig. 15b**). For clarity, we include greater detail around the COOH modes (Supplementary **Fig. 15c,d,e**) for both spectra. As discussed above, when a pyridyl group rotates out of the terpyridine plane and H_2O is bound to the structure, some terpyridine vibrations that were previously degenerate are split and broadened due to the loss of symmetry. This is also true for COOH bound to the nickel centre and is particularly evident in the low wavenumber region of the spectra. Two δ(O-C-O) modes are highlighted in Supplementary **Fig. 15c** at 424 cm^{-1} and 640 cm^{-1}. For the same reasons above, both modes partially overlap with modes of the pyridyl rings, shown here with (*). We highlight δ(H-O-C) in (Supplementary **Fig. 15d**) occurring close to a mixed mode of the pyridyl groups that involves asymmetric ω(C-H) and ν(C-C) character. In this case, better separation of the vibrations of the bidentate and tridentate terpyridines shows how these modes blueshift in structure **4b** compared with **2w**. We hence observe the clearly distinguished COOH mode at 1254 cm^{-1}. The ν(C=O) mode is highlighted in Supplementary **Fig. 15e** and a discussion about the intensity of this peak is included in response to the following question. We observe this peak to occur at 1740 cm^{-1} in a region that is not overlapped by other modes.

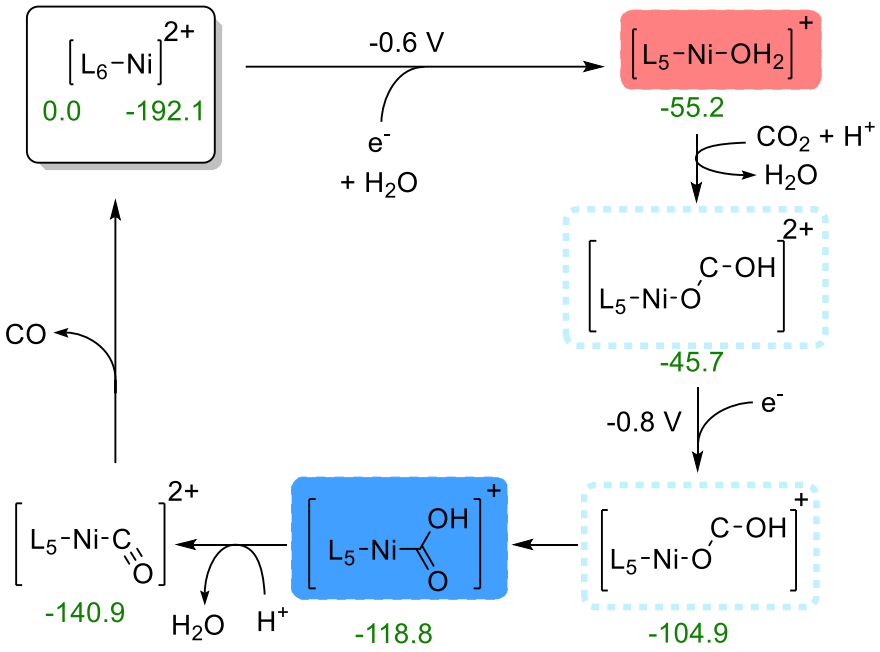

Supplementary Fig. 16 | Extended catalytic cycle for **Ni(tpyS)$_2$** including the energetically most favourable non-coupled proton and electron transfer steps that are not observed experimentally. Energies are in kcal mol^{-1}.

Supplementary Note 6 | Geometrical estimate of molecules in hotspot

We calculate the full width at half maximum (FWHM) of the hotspot in NPoM by[11]

$$\text{FWHM} = \sqrt{\frac{Dd}{n}} \tag{3}$$

where, d (gap thickness) = 1.5 nm, n (gap refractive index) = 1.4, D (nanoparticle diameter) = 60. This gives a FWHM value of 8.0 nm.

Using a computational estimate for spacing of similar molecules to those here on Au,[12] we reach a value of approximately 17 molecules in the hotspot that contribute the majority to the SERS signal.

Alternatively using the geometric footprint of **Ni(tpyS)$_2$**, if we assume that each **Ni(tpyS)$_2$** occupies a square, 1.56 nm^2 is the surface area for one molecule. Using this as a packing parameter, we arrive at an estimate of 32 molecules in the hotspot.

Supplementary Note 7 | Further catalytic cycle discussion

The catalytic cycle presented in the main text **Fig. 4b** represents the best mechanism combining computational and experimental spectroscopic information for the present catalytic cycle. In addition, we also present Supplementary **Fig. 16,** which includes two additional intermediates that were not spectroscopically verified but are supported by computational results. This mechanism highlights the computational results that in certain conditions, a Ni-O bound intermediates might form when CO_2 first interacts with nickel centre before the more stable Ni-C species is formed. These potential intermediates might be too short-lived to be observed experimentally. It is difficult to prove or disprove a concerted electron and proton transfer based on our results, nevertheless, we can exclude that the proton transfer precedes the reduction step based on the calculated free energies. Moreover, before the second electron transfer occurs, structures with nickel centre bound *via* a CO_2 oxygen atom become energetically stable (**3a,c** in Supplementary **Fig. 11d)**. This indicates that under such conditions, a nucleophilic oxygen atom can attack the exposed nickel centre and result in Ni-O bound species. After the second electron transfer, the more thermodynamically stable Ni-C species is recovered by an η^2 electron transfer step. This mechanism and discussion is provided as an interesting observation emerging from computational results that offers scope for further study.

Supplementary References

1. Schneider, C. A., Rasband, W. S. & Eliceiri, K. W. NIH Image to ImageJ: 25 years of image analysis. *Nat. Methods* **9**, 671–675 (2012).
2. Foster, J. P. & Weinhold, F. Natural hybrid orbitals. *J. Am. Chem. Soc.* **102**, 7211–7218 (1980).
3. Reed, A. E., Weinstock, R. B. & Weinhold, F. Natural population analysis. *J. Chem. Phys.* **83**, 735–746 (1985).
4. Reed, A. E. & Weinhold, F. Natural localized molecular orbitals. *J. Chem. Phys.* **83**, 1736–1740 (1985).
5. Kline, J. Properties of the d-dimensional earth mover's problem. *Discret. Appl. Math.* **265**, 128–141 (2019).
6. Dobrushin, R. Prescribing a system of random variables by conditional distributions. *Theory Probab. its Appl.* **15**, 458–486 (1970).
7. Song, J., Klein, E. L., Neese, F. & Ye, S. The mechanism of homogeneous CO_2 reduction by Ni(cyclam): Product selectivity, concerted proton-electron transfer and C-O bond cleavage. *Inorg. Chem.* **53**, 7500–7507 (2014).
8. Tissandier, M. D. *et al.* The proton's absolute aqueous enthalpy and Gibbs free energy of solvation from cluster-ion solvation data. *J. Phys. Chem. A* **102**, 7787–7794 (1998).
9. Linnell, R. Notes- Dissociation Constants of 2-Substituted Pyridines. *J. Org. Chem.* **25**, 290 (1960).
10. Farkas, E., Enyedy, É. A., Micera, G. & Garribba, E. Coordination modes of hydroxamic acids in copper(II), nickel(II) and zinc(II) mixed-ligand complexes in aqueous solution. *Polyhedron* **19**, 1727–1736 (2000).
11. Savage, K. J. *et al.* Revealing the quantum regime in tunnelling plasmonics. *Nature* **491**, 574–577 (2012).
12. Morari, C., Rungger, I., Sanvito, S., Melinte, S. & Rignanese, G. Charge and spin transport in single and packed ruthenium-terpyridine molecular devices : Insight from first-principles calculations. *Sci. Rep.* **6**, 31856 (2016).